

## Deep anoxic aquifers could act as sinks for uranium through microbial-assisted mineral trapping

Ivan N. Pidchenko<sup>1✉</sup>, John N. Christensen<sup>2</sup>, Martin Kutzschbach<sup>3</sup>, Konstantin Ignatyev<sup>4</sup>, Ignasi Puigdomenech<sup>5</sup>, Eva-Lena Tullborg<sup>6</sup>, Nick M. W. Roberts<sup>7</sup>, E. Troy Rasbury<sup>8</sup>, Paul Northrup<sup>8</sup>, Ryan Tappero<sup>9</sup>, Kristina O. Kvashnina<sup>10,11</sup>, Thorsten Schäfer<sup>12</sup>, Yohey Suzuki<sup>13</sup> & Henrik Drake<sup>1</sup>

Uptake of uranium (U) by secondary minerals, such as carbonates and iron (Fe)-sulfides, that occur ubiquitously on Earth, may be substantial in deep anoxic environments compared to surficial settings due to different environment-specific conditions. Yet, knowledge of U reductive removal pathways and related fractionation between <sup>238</sup>U and <sup>235</sup>U isotopes in deep anoxic groundwater systems remain elusive. Here we show bacteria-driven degradation of organic constituents that influences formation of sulfidic species facilitating reduction of geochemically mobile U(VI) with subsequent trapping of U(IV) by calcite and Fe-sulfides. The isotopic signatures recorded for U and Ca in fracture water and calcite samples provide additional insights on U(VI) reduction behaviour and calcite growth rate. The removal efficiency of U from groundwater reaching 75% in borehole sections in fractured granite, and selective U accumulation in secondary minerals in exceedingly U-deficient groundwater shows the potential of these widespread mineralogical sinks for U in deep anoxic environments.

<sup>1</sup>Department of Biology and Environmental Science, Linnaeus University, SE-39182 Kalmar, Sweden. <sup>2</sup>Energy Geosciences Division, Lawrence Berkeley National Laboratory, Berkeley, CA 94720, USA. <sup>3</sup>Fachgebiet Angewandte Geochemie, Technische Universität Berlin, 10587 Berlin, Germany. <sup>4</sup>Diamond Light Source, Harwell Science and Innovation Campus, Didcot OX11 0QX Oxon, UK. <sup>5</sup>Swedish Nuclear Fuel and Waste Management Co. (SKB), Box 3091, SE-16903 Solna, Sweden. <sup>6</sup>Terralogica AB, Östra Annedärrsvägen 17, SE-44372 Gråbo, Sweden. <sup>7</sup>Geochronology and Tracers Facility, British Geological Survey, Nottingham NG12 5GG, UK. <sup>8</sup>Department of Geosciences, FIRST, Stony Brook University, 100 Nichols Rd, Stony Brook, NY 11794, USA. <sup>9</sup>Photon Sciences Department, National Synchrotron Light Source, Brookhaven National Laboratory, Upton, New York, NY 11973, USA. <sup>10</sup>Helmholtz-Zentrum Dresden-Rossendorf, Institute of Resource Ecology, P.O. Box 510119, D-01314 Dresden, Germany. <sup>11</sup>The Rossendorf Beamline at ESRF - The European Synchrotron, CS40220, 38043 Grenoble Cedex 9, France. <sup>12</sup>Applied Geology, Institute for Geosciences, Friedrich-Schiller-University Jena, 07749 Jena, Germany. <sup>13</sup>Graduate School of Science, The University of Tokyo, Tokyo 113-8654, Japan. ✉email: [ivan.pidchenko@lnu.se](mailto:ivan.pidchenko@lnu.se)

Uranium (U) is a ubiquitous trace element occurring in low-temperature carbonate minerals, sediments and rocks. These carbonate materials containing U are extensively used for fundamental investigations, including geochronology, oceanic paleo-redox studies, and environmental proxies. The latter studies use  $^{238}\text{U}/^{235}\text{U}$  isotope fractionation signature ( $\delta^{238}\text{U}$ ) as a specific proxy for redox and coupled climate changes throughout Earth's geological history<sup>1–6</sup>. In contrast, only a limited number of  $\delta^{238}\text{U}$ -studies constrain local environmental impacts after engineering activities, such as U mining and related redox perturbations<sup>7–9</sup>. Since considerable U isotope fractionation is expected, mainly during U(VI) reduction, systems that include abundant redox-active species, e.g., iron (Fe)-sulfides, have attracted the most interest. The occurrence of elevated U as U(IV) has been reported from a few U-rich ancient calcites<sup>10–12</sup>, but no U isotope fractionation analyses have yet been reported for these systems. It has been proposed that a high partition coefficient of U detected in anoxic systems might result from structurally incorporated U(IV) in secondary minerals<sup>13</sup>. However, this is yet unconfirmed as no coupled proof exists for the occurrence of structural U(IV) in calcite formed under reducing conditions, coupled with a high partition coefficient attested by water and mineral analyses.

Recent laboratory studies have aimed to better understand U isotope fractionation mechanisms that would link  $\delta^{238}\text{U}$  signatures to local and global redox conditions<sup>14,15</sup>. However, these links remain elusive and underexplored when applied to deep anoxic, microbial-mediated rock environments. Current estimates show that the deep biosphere hosts the majority of microbial life on Earth and a substantial amount of biomasses<sup>16</sup>. Since microbes catalyze the decomposition of organic substances, facilitating the formation of secondary minerals, such as calcite<sup>13,17</sup> and Fe-sulfides<sup>18,19</sup>, and thus affect the environmental mobility of trace elements such as U, there is an urgent need for exploring microbially mediated U reduction and related U isotope fractionation in subsurface settings. A recent study has reported the formation of non-crystalline U(IV) species formed in a roll-front deposit after microbial activity based on the finding of positive  $\delta^{238}\text{U}$  signatures<sup>9</sup>. While the latter and other recent studies have focused on either ancient systems in various natural samples<sup>1,3,10,11,20–23</sup>, or laboratory experiments<sup>24–26</sup> (relevant publications are shown in Supplementary Information (SI) and Supplementary Table 1), investigations of modern carbonates, involving analysis of  $\delta^{238}\text{U}$  signatures linked to U speciation in diluted environmental systems are scarce.

Herein, we aim to explore how  $\delta^{238}\text{U}$  is associated with U incorporation into calcite in a deep anoxic, igneous-rock fracture network-hosted groundwater aquifer at the Äspö Hard Rock Laboratory (HRL), south-eastern Sweden. Over 17 years, calcite has precipitated along with Fe-sulfides on borehole equipment in an isolated deep borehole section and immobilized large portions of U from groundwater during precipitation (Supplementary Fig. 1a–d). A recent study performed on these calcite specimens showed that U (along with some other trace elements) exhibits unexpectedly high distribution coefficients, implying that U redox transformation processes aiding co-precipitation with calcite have occurred in the borehole<sup>13</sup>. As both the source (groundwater) and sink (calcite) can be examined in this borehole section, and because the system is influenced by bacterial sulfate reduction, dissolved sulfide ( $\text{HS}_{(\text{aq})}^-$ ) and ferrous ( $\text{Fe(II)}_{(\text{aq})}$ ) species, and Fe-sulfidic precipitates, this system is optimal for assessing U speciation and isotope fractionation related to a complex natural system that involves both abiotic and biotic redox mediators. This is an important complement to laboratory experiments that investigate more simplified systems with individual biotic and abiotic redox species<sup>14,15,27</sup>. In this study, we use a suite of

micro-analytical synchrotron-based and laboratory techniques, U and Ca isotopic tools, and thermodynamic modeling to reveal U speciation, redox evolution, removal pathways, and related isotope fractionation in the deep subsurface.

## Results

**Uranium speciation in calcite.** Synchrotron micro-X-ray fluorescence ( $\mu\text{XRF}$ ) mapping coupled to U  $L_{\text{III}}$ -edge micro-X-ray absorption near edge structure ( $\mu\text{XANES}$ ) spectroscopy, as well as an extended X-ray absorption fine structure (EXAFS) technique, were used to reveal U distribution, U oxidation state and the local atomic environment in “Äspö-calcite” material. The U  $\mu\text{XRF}$  map recorded on a  $200\ \mu\text{m} \times 300\ \mu\text{m}$  area of one “Äspö-calcite” crystal is shown in Fig. 1a with  $\mu\text{XANES}$  spectrum collected on a  $30\ \mu\text{m} \times 100\ \mu\text{m}$  region of the U-rich rim, together with spectra of U(IV)-calcite and U(VI)-calcite (Fig. 1b), and Fourier-transformed (FT) EXAFS data for “Äspö-calcite” (Fig. 1c).

The “Äspö-calcite” XANES spectrum exhibits the position and shape of main resonances at nearly 17,176 eV and broader post-edge peaks around 17,216 eV, which perfectly agree with those for the “U(IV)-calcite” spectrum—a well-studied U(IV)-bearing calcite material collected from a high-U anoxic Mississippi

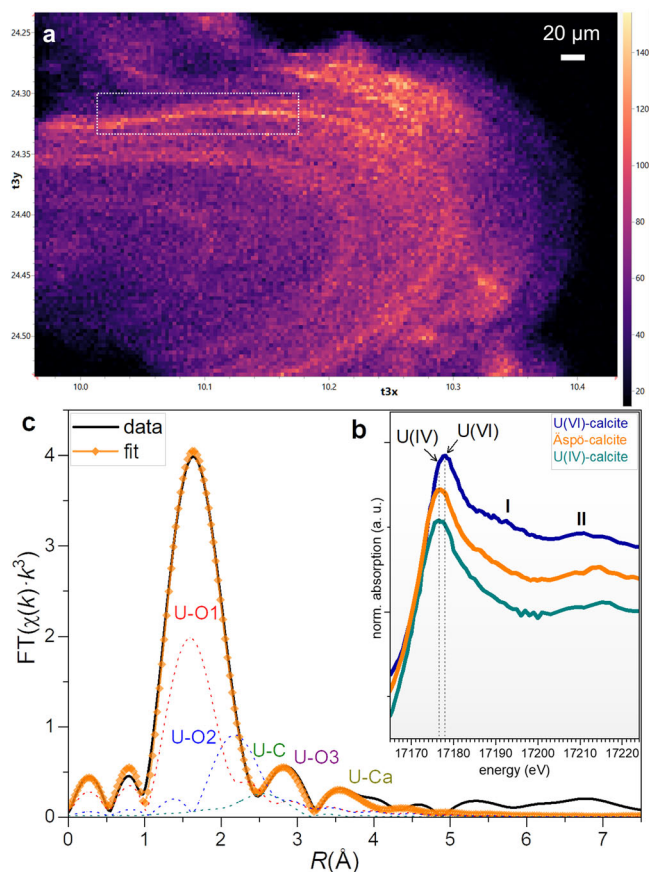


**Fig. 1**  $\mu\text{XRF}$  and  $\mu\text{XAS}$  results. **a** U  $\mu\text{XRF}$  map of a calcite crystal from Äspö HRL. The area outlined with a dashed line was used for U  $L_{\text{III}}$ -edge XANES measurements (estimated  $\sim 20$  ppm U<sup>13</sup>, on the right y-axis - relative signal intensity scale); **b** U  $L_{\text{III}}$ -edge  $\mu\text{XANES}$  spectra of Äspö-calcite, U(IV)-calcite<sup>11</sup> and U(VI)-calcite<sup>20</sup>. The energy shift between U(IV) and U(VI) references is  $\sim 1.6$  eV. Marked on the spectrum of ‘U(VI)-calcite’ with I and II are spectral features characteristic to uranyl(VI) species; **c** Magnitude of the Fourier-transformed EXAFS (black solid line) and best fit (colored rhombs) for the “Äspö-calcite” and single scattering paths for the fitted shells (see further details in SI and Supplementary Fig. 2c, d for  $k^3$ -weighted and the real part EXAFS data).

Valley-type zinc ore deposit<sup>11</sup>. Distinct spectral features characteristic to U(VI), such as a main resonance peak shifted nearly 2 eV to higher energy at ~17,178 eV, a ‘shoulder’ feature at ~17,190 eV (marked as I), and a less intense peak with a maximum around 17,210 eV (marked as II), which are usually assigned to uranyl species<sup>28</sup> can be distinguished on the spectrum of “U(VI)-calcite” used as a U(VI) reference and is described elsewhere<sup>20</sup>. The  $\mu$ XAS measurements at two different microfocus beamlines showed similar results (see Supplementary Figs. 2a,b), and  $k^3$ -weighted  $\chi(k)$  and the real part of the FT-EXAFS (Supplementary Figs. 2c,d). Additionally, the same calcite material was analyzed by U L<sub>III</sub>-edge high-energy resolution fluorescence-detected XANES spectroscopy, which showed the bulk occurrence of U(IV) (Supplementary Fig. 3). Linear combination fit (LCF) analysis gave  $94 \pm 3\%$  for U(IV) and  $6 \pm 3\%$  for U(VI) fractions. Additional EXAFS fit was performed, including three U-O shells for the first intense FT-EXAFS peak, aiming to determine the possible contribution from the uranyl(VI) group. The yielded  $1.74(2) \text{ \AA}$  is inconsistent with any reported axial U-O bond in uranyl(VI) compounds<sup>29</sup>. FT-EXAFS of “Äspö-calcite” is better described with a two U-O shell approach for the main peak with U-O1 at  $2.22(2) \text{ \AA}$  and U-O2 at  $2.82(3) \text{ \AA}$ , and nearly equal coordinating oxygens,  $3.1(4)$  and  $2.7(5)$ , respectively (Table 1). The further backscattering peak is well fitted with equal contribution from carbonates: (U-C) at  $3.30 \text{ \AA}$  and (U-O3) at  $3.52 \text{ \AA}$ , indistinguishable from each other, and more distant low-intensity backscattering peak at  $4.07(7) \text{ \AA}$ , referring to U-Ca shell.

**Uranium isotope fractionation signatures in groundwater and calcite.** U isotope values ( $\delta^{238}\text{U}$ ), U-series activity ratio ( $\text{AR} = {}^{234}\text{U}/{}^{238}\text{U}$ ), and the U concentrations measured for calcite and water samples are given in Table 2. Both borehole-section specific pairs of calcites (calcite1 and calcite2) and fracture water samples (FW1 and FW2) exhibit strong  $^{238}\text{U}$  depletion, at  $\delta^{238}\text{U} \sim -2\%$ , and thus, insignificant net fractionation  $\Delta^{238}\text{U}_{\text{calcite1-FW1}}$  of  $\sim 0.11\%$  and  $0.03\%$  (Fig. 2), within the  $0.12\%$  uncertainty. A third calcite sample from a separate packed-off section in the same borehole (no corresponding water sample available) showed a similar value as  $\delta^{238}\text{U}_{\text{calcite2}}$ . The  ${}^{234}\text{U}/{}^{238}\text{U}$  AR were relatively high and showed small variations within 4.47–4.87 (Table 2).

Calcium isotope composition ( $\delta^{44}\text{Ca}$ ) determined for both calcite and borehole water samples revealed an average calcite-water difference  $\Delta^{44/40}\text{Ca}_{\text{c-w}}$  of  $-0.43\%$  (Supplementary Fig. 4). Using the observed thickness (average  $500 \mu\text{m}$ ) and a volume of calcite ( $3.5 \times 10^{-5} \text{ dm}^3$ ) for one of the calcite samples and duration of 17 years, an estimated calcite growth rate of  $2.5 \times 10^{-8} \text{ moles/m}^2/\text{sec}$  can be calculated. Together with the  $\Delta^{44/40}\text{Ca}_{\text{c-w}}$  of  $-0.43\%$  this is consistent with the surface kinetic model describing the relationship between calcite growth rate and Ca isotope fractionation, as well as with experimental data at higher growth rates<sup>30</sup> (Supplementary Fig. 5). Our observed  $\Delta^{44/40}\text{Ca}_{\text{c-w}}$  and  $\text{Ca}^{2+}/\text{CO}_3^{2-}$  ratios are compared to predicted curves for different values of calcite super-saturation<sup>31</sup> (Supplementary Fig. 6). The position of our data for the growth of calcite falls along the curve for  $\sigma = 0.5$ , in a good agreement with the calculated median value of 0.46 for the growth conditions in the boreholes. The consistency of our data shown in Supplementary Figs. 5, 6 indicates, on average, essentially continuous calcite growth over the 17-year period of the experiment at low calcite supersaturation. The well-preserved growth zones in calcite agree with the groundwater sampling events and the variation of Sr content in the calcite that reflects the change of water chemistry (increased fraction of Baltic Seawater) during the

**Table 1 EXAFS fit results for the “Äspö-calcite” sample.**

SP	N	R, Å	$\sigma^2, \text{Å}^2$
U-O1	3.2(3)	2.22(2)	0.0006(4)
U-O2	2.8(4)	2.82(3)	0.0006(4)
U-C	6.0*	3.30(5)	0.0174(5)
U-O3	6.0*	3.52(7)	0.0174(5)
U-Ca	6.0*	4.07(7)	0.0401(9)

The goodness of fit- 0.2% was achieved, and the energy shift,  $\Delta E_0 = -9.4(3) \text{ eV}$ . SP scattering path, N coordination number, R bond distance,  $\sigma^2$  Debye-Waller factor. \* - fixed value. The uncertainty is shown in parentheses for the last digit at  $1\sigma$ .

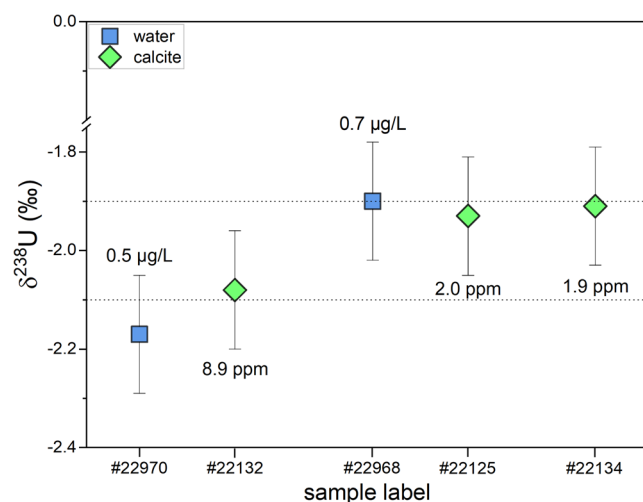


**Fig. 2  $\delta^{238}\text{U}$  in waters and solids.**  $\delta^{238}\text{U}$  in fracture water (blue squares) and calcite (green rhombs) samples collected from the borehole equipment at 415 m depth in KA3105A borehole, Äspö. FW #22970 refers to calcite #22132 and FW #22968 refers to calcite #22125. For calcite sample #22134, no water sample is available. Dashed lines at  $-1.90\%$  and  $-2.10\%$  are plotted for reference relevant to the fluid-solid setting. Error bars represent  $\delta^{238}\text{U} = 0.12\%$  as  $\pm 2\sigma$ .  $\delta^{238}\text{U}$  values for modern continental crust and seawater are  $-0.29(3)\%$  ( $2\sigma$ ) and  $-0.39(1)\%$  ( $2\sigma$ ), respectively<sup>90</sup>.

**Table 2 U content,  $\delta^{238}\text{U}$  and  ${}^{234}\text{U}/{}^{238}\text{U}$  measured in calcite and fracture water (FW) samples, collected from borehole sections at Äspö HRL.**

Sample, ID	U, $\mu\text{g/L}$	U, ppm	$\delta^{238}\text{U}, \%$	${}^{234}\text{U}/{}^{238}\text{U}$ , activity ratio
FW1, #22970	0.47	—	-2.17	4.8728
FW2, #22968	0.71	—	-1.90	4.8402
Calcite1, #22132	—	8.86	-2.08	4.4693
Calcite2, #22125	—	2.03	-1.93	4.6996
Calcite3, #22134	—	1.95	-1.91	4.8320

FW #22970 refers to calcite #22132 and FW #22968 refers to calcite sample #22125. No FW is available for calcite sample #22134. Uncertainties at  $\pm 2\sigma$  are for  $\delta^{238}\text{U} = 0.12\%$  and for  $\text{AR } {}^{234}\text{U}/{}^{238}\text{U} = 0.0015$  u.

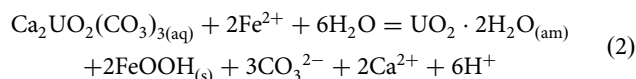
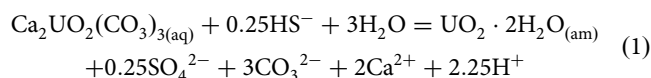
experiment, supporting the  $\Delta^{44/40}\text{Ca}_{\text{c-w}}$  data for the continuous growth of calcite<sup>13</sup>. However, this does not preclude short periods of more rapid calcite growth (or dissolution), involving the production of the high-U small-scale (tens of microns) laminations.

## Discussion

**Uranium speciation in calcite.** The  $\mu$ XRF analysis shows an uneven distribution of U within and between the different growth zones, from 2 ppm up to 20 ppm in the brighter part of a calcite sample with median U at  $\sim 9$  ppm U. Relatively U-rich zonation that occurs at regular intervals can be attributed to water sampling activities when an inflow of pristine fracture water with a higher U content replaced flushed out stagnant water. This semi-closed cycle that follows flushing out of ten section volumes starts with high incorporation of U, and as partitioning of U(IV) is high, the calcite will become successively poorer in U with time, resulting in the varying U content in the precipitating calcite. Direct spectroscopic determination of U(IV) in calcite at a relatively high U content is in accordance with two previous studies that demonstrated the incorporation of U(IV) into ancient carbonates of various settings<sup>10,11</sup>. Since high U partition coefficients ( $p_u \sim 100$ ) have been determined for the calcite samples used in the current study<sup>13</sup>, we can here confirm, based on EXAFS results, the previous hypothesis that partitioning of U into calcite is governed by structural incorporation of U(IV). This observation is further supported by the absence of the peak at 3.83–3.86 Å relevant to the U-U backscattering peak observed in  $UO_2$ . There is neither any evidence for the short U-O shell, which is normally resolved in an EXAFS spectrum as an intensive peak at 1.8 Å, nor for the longer U-O shell characteristic for equatorial bonds from 2.3 to 2.5 Å<sup>29</sup>. U-O backscattering peak of some uranyl(VI) species, e.g., U(VI) on calcium silicate hydrates<sup>32</sup>, may appear as a broad backscattered peak to some degree resembling the U-O in our EXAFS data. The clear evidence of U(IV) from  $\mu$ XANES data supported by LCF analysis rules out the possibility of U(VI) stabilization in the “Äspö-calcite”. Nearly 6% of U(VI) derived from LCF analysis can be referred to as statistical error due to spectral noise. EXAFS results for U-O1 and U-O2 shells agree well with the previously analysed U(IV)-calcite material for U-O1 at 2.21(3) Å and U-O2 at 2.78(2) Å<sup>11</sup>. The local coordination environment of U(IV) in calcite can be described with two models assuming different contributions of shorter (U-O1) and longer (U-O2) shells with ratios 4:2 and 3:3 that result in statistically indistinguishable mean U-O distances at 2.42 Å and 2.52 Å, respectively. Both calculated U-O values are in the range of U-O distances (2.35–2.49 Å) for some U(IV) compounds<sup>11</sup> and notably larger than mean U-O distances (2.1–2.3 Å) for uranyl(VI) compounds<sup>33</sup>. A relatively high amount of Na (200–900 ppm) detected in the “Äspö-calcite” sample<sup>13</sup> is theoretically enough to stabilize  $U^{4+}$  in the calcite through an earlier proposed charge compensation mechanism:  $3Ca^{2+} = U^{4+} + 2Na^+$ , that achieves local charge balance in the crystal lattice<sup>11</sup>. The EXAFS data is complemented by high-resolution field emission electron probe micro-analysis (FE-EPMA), which shows the relationship of several major and trace elements (Supplementary Fig. 7). The technique was described recently to detect coffinite-like U(IV) nanoclusters formed and preserved in ancient calcite<sup>34</sup>. No evidence of individual  $UO_2$  microphases or nanoparticles was found in the present study, supporting EXAFS results for U incorporation into the calcite crystal lattice as indicated by the above observations. Structural incorporation of U(IV) into calcite is evidently an effective mechanism for long-term immobilization of U from groundwater under anoxic conditions, even for exceedingly U-deficient groundwater near the solubility limit of  $UO_{2(am)}$ .

**Redox evolution in borehole water.** An estimation of U redox speciation in the borehole water,  $[U] \sim 10^{-9}$  mol/L, was done with the available geochemical data for the KA3105A borehole using PHREEQC<sup>35</sup>. The modeling shows a correlation between

the calculated fraction of U(IV) and the reducing agents and their concentrations in the groundwater: either dissolved hydrogen sulfide ( $HS^-_{(aq)}$ ) at  $4.3 \times 10^{-6}$  mol/L or dissolved ferrous ( $Fe(II)_{(aq)}$ ) species at  $5.4 \times 10^{-6}$  mol/L (Supplementary Table 2). PHREEQC reaction path calculations predict a redox-related evolution of U speciation based on the  $HS^-$  concentration in the borehole water. Aquatic modeling of Äspö groundwaters have shown that thermodynamically stable U(VI) complexes are the main species that occur in this deep aquifer, with up to 4% of U(IV) present as hydrolyzed species<sup>13</sup>. The persistence of U(VI) under the reducing conditions (redox potential,  $E_h \sim -270$  mV) dominating in fracture water can be attributed to the formation of thermodynamically stable U(VI) complexes, such as  $Ca_2UO_2(CO_3)_3(aq)$ . There is virtually no available speciation technique for direct U redox determination at the extremely low U concentration ( $[U] \sim 10^{-9}$  mol/L) measured in the KA3105A borehole water that is near the solubility limit of  $UO_{2(am)}$ <sup>36</sup>. Depending on the U concentration and main geochemical parameters (pH,  $E_h$ , ionic strength, dissolved inorganic carbon, and Ca), the U(VI) reduction may result in the precipitation of  $UO_2$ , usually represented as amorphous hydrate,  $UO_2 \cdot 2H_2O_{(am)}$ <sup>36</sup>. The PHREEQC speciation calculations predict that in the KA3105A borehole water, U occurs predominantly as aqueous U(VI) species but with a minor fraction of aqueous U(IV) species<sup>13</sup>. Under this condition, the concentration of U(IV) is too low for  $UO_2 \cdot 2H_2O_{(am)}$  to precipitate, while the removal of U(IV) by coprecipitation with calcite is energetically favorable. The occurrence of high  $Fe(II)_{(aq)}$  relative to dissolved U(VI) is expected to facilitate the reduction of U(VI) in borehole water<sup>37</sup>, where slow fluid exchange favors elevated concentrations of dissolved species that promotes precipitation of Fe-sulfides. Laboratory experiments show that U(VI)-carbonate complexes are more readily reduced to U(IV) on the surface of Fe(II) minerals<sup>38,39</sup>, by  $HS^-_{(aq)}$ <sup>40</sup> or with  $Fe(II)_{(aq)}$ <sup>37</sup> making these routes thermodynamically feasible in stagnant water in the borehole setting. The simultaneous presence of both  $Fe(II)_{(aq)}$  and  $HS^-_{(aq)}$  in the water, and limitations for measuring redox potential in the sulfidic system, e.g., fouling of electrode surface<sup>41</sup>, set certain complications to experimentally determine the redox effect from the individual species. Although measurements of the redox potential for this borehole section are not available, according to PHREEQC calculations, the redox potential for borehole water corresponding to the KA3105A section is found lower for the  $HS^-/SO_4^{2-}$  as compared with the Fe(II)/Fe(III) couple for low concentration of redox species. The reducing capacity of these two species can be understood from redox equations, where eight times less sulfide (Eq. 1) compared to ferrous iron are consumed for the reduction of 1 mole of U(VI) to U(IV) (Eq. 2). Thus,  $Fe(II)_{(aq)}$  can be considered as a moderate reducer while  $HS^-_{(aq)}$  is a strongly reducing species<sup>42</sup>.



The redox potentials for these two systems depend on pH, as well as on the concentrations of the reducing species, and therefore, the U(VI)/U(IV) ratio calculated according to either  $HS^-_{(aq)}$  or  $Fe(II)_{(aq)}$ , will also depend on pH and on the concentrations of  $HS^-_{(aq)}$  or  $Fe(II)_{(aq)}$ . For the investigated borehole section, the calculated  $E_h$  is slightly higher for the sulfide-sulfate system ( $E_h = -217$  mV) than for the Fe(II)/Fe(III) system ( $E_h = -270$  mV), resulting in a larger U(VI)/U(IV) ratio calculated for the sulfide redox system, even when the reducing

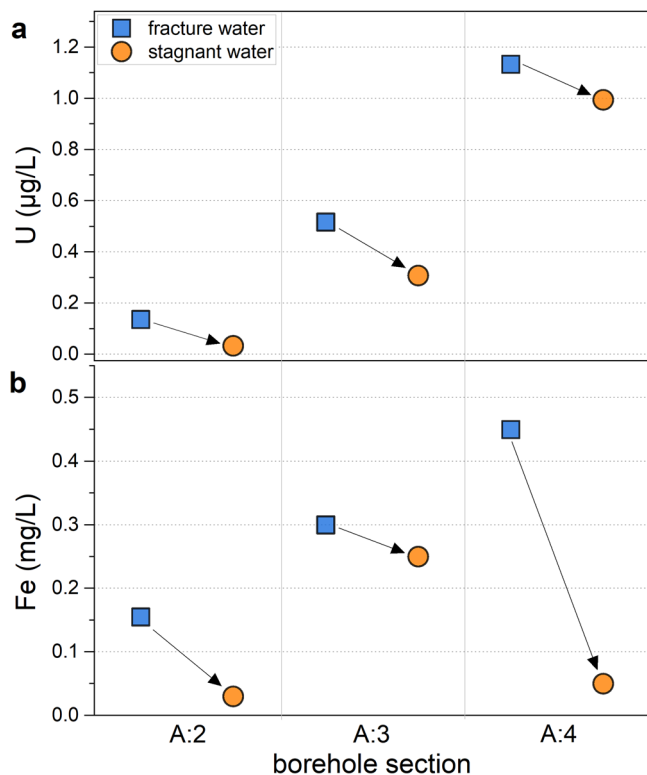


**Fig. 3** Uranium and iron variation in waters. **a** U and **b** Fe concentration in fracture water (blue squares) vs stagnant water (orange circles) in monitored A:2, A:3, and A:4 sections in KA3105A borehole based on analysis of the final water withdrawal (see Supplementary Table 3).

capacity of the sulfide is larger than that of  $\text{Fe(II)}_{(\text{aq})}$  (Supplementary Table 2).

### Uranium turnover and removal pathways in deep aquifers.

Dissolved U concentrations at the site decrease in groundwater by more than 1 order of magnitude from the highest measured of 7 µg/L at 31 m to ~0.3 µg/L in 600 m deep borehole sections<sup>43</sup>. There is thus a systematic removal of U from the groundwater along its flow path, associated with continuous interaction of mobile U(VI) with redox fronts on deep fracture mineral surfaces that can be a key mechanism resulting in a decrease of U concentration in Äspö groundwaters from shallow to deep aquifers<sup>43–45</sup>.

The studied Äspö HRL borehole sections represent semi-closed systems where fracture water constantly flows through and partly resides as stagnant water. Hence, it is important to estimate the U mass balance for the interpretation of the U reductive removal and related isotopic fractionation. It should be noted that time-dependent groundwater compositions and U concentrations are not available for the 17-year time span of the experiment; hence it is not possible to provide chemical rate constants from our results. Previous laboratory studies have indicated that primarily uranyl non-carbonate species control the kinetics of the bio-reduction rate of U(VI) to U(IV)<sup>46</sup>. If the fracture water flow rate through the borehole was not subject to considerable variations, one can approximate the U mass balance during the 17 years of the experiment using simplified calculations, which do not consider the removal of solid phases by water flow or precipitation on borehole walls (Supplementary Table 3).

The U mass (in mg) that passed through the A:3 borehole was about 3.1 mg of U, of which 1.25 mg is removed in the

borehole. The amount of groundwater passed through the A:3 section is estimated at 5900 L, which is 1000 times the volume of the A:3 section<sup>47</sup>. In the same way, the turnover U amounts can be estimated for A:2 and A:4 borehole sections resulting in 2 and 5.92 mg, respectively. The Fe turnover is nearly three orders of magnitude higher than U for each borehole section. The removal of dissolved U in the borehole water is accompanied by the decrease of dissolved Fe. The removal efficiencies for U and Fe vary in the borehole sections; 75% in A:2, 40% in A:3, and 12% in A:4 (Fig. 3a) and ca. 80% in A:2, 17% in A:3, and 89% in section A:4 (Fig. 3b), respectively. The joint decrease of U and Fe from the borehole water might be due to a coupled reduction of U(VI) with sulfides and subsequent incorporation into the structure of calcite, further based on observations of surface U clusters forming on Fe-sulfides mixed with calcite crystals.

The laser ablation inductively coupled plasma mass spectrometry (LA-ICP-MS) analysis of Fe-sulfide coatings formed on magnetite crystals shows that U is associated primarily with Fe-sulfide forming on the surface of magnetite<sup>48</sup> (Fig. 4a) with U concentration reaching ~90 ppm in few spots forming on the mineral grain boundary (Fig. 4b, c). The finding of this relatively high amount of U on the surface of Fe-sulfide is remarkable, given that U concentration in fracture water is at ~10<sup>-9</sup> mol/L, under dynamic conditions where fracture water continuously passes through the borehole.

The environmental behavior of U is controlled by several processes, including complexation, adsorption, precipitation, and redox transformations, and often followed by structural incorporation in secondary minerals, e.g., earth-alkali metal carbonates, Al- and Fe-oxyhydroxides<sup>49</sup>. While both U(IV) and U(VI) are removed by carbonates primarily through structural incorporation as shown for calcite in this work and in previous studies<sup>11,20</sup>, Fe-oxyhydroxides may exhibit several U removal pathways, e.g., adsorption of U(VI) species onto mineral surface followed by the formation of  $\text{UO}_2$  precipitates<sup>50</sup> or structural incorporation of various U redox species<sup>51,52</sup>. Based on the LA-ICP-MS results, U has accumulated on the surface of Fe-sulfide, which in turn is formed on magnetite formed during the corrosion of borehole equipment. Sulfidization of magnetite occurs due to microbially-driven production of  $\text{HS}^-_{(\text{aq})}$ , enhanced in stagnant water under relatively slow water inflow conditions. In Äspö groundwater, U occurs as soluble U(VI)-carbonate complexes, which can be readily removed by Fe-sulfides via selective adsorption followed by fast reduction to U(IV), as shown in laboratory batch experiments<sup>53,54</sup>, and detailed reaction mechanisms proposed elsewhere<sup>55</sup>. U speciation was not analysed for Fe-sulfide material due to technical reasons. It is reasonable to anticipate that U occurs as  $\text{UO}_2$  stabilized on the surface of Fe-sulfide, in accordance with several laboratory studies<sup>53–57</sup>. The stability of the precipitated  $\text{UO}_2$  depends on several factors, including the redox sink of the mineral phase, e.g., Fe-sulfides, the persistence of reducing and anoxic conditions, and a limited supply of reactants to maintain redox processes.

**Evidence for microbial organic phase degradation.** The elevated sulfide concentrations in the borehole can be explained by sulfate-reducing bacteria (SRB) degrading dissolved organic species in water and plasticizers included in polyvinylchloride (PVC) tape used to fasten the water collection equipment. Bis(2-ethylhexyl) phthalate (or DEHP, chemical formula –  $\text{C}_{24}\text{H}_{38}\text{O}_4$ ) is one of the most common plasticizers, which is added to make the plastics flexible. DEHP is known to be readily biodegraded by bacteria in water and sediments<sup>58</sup> and to

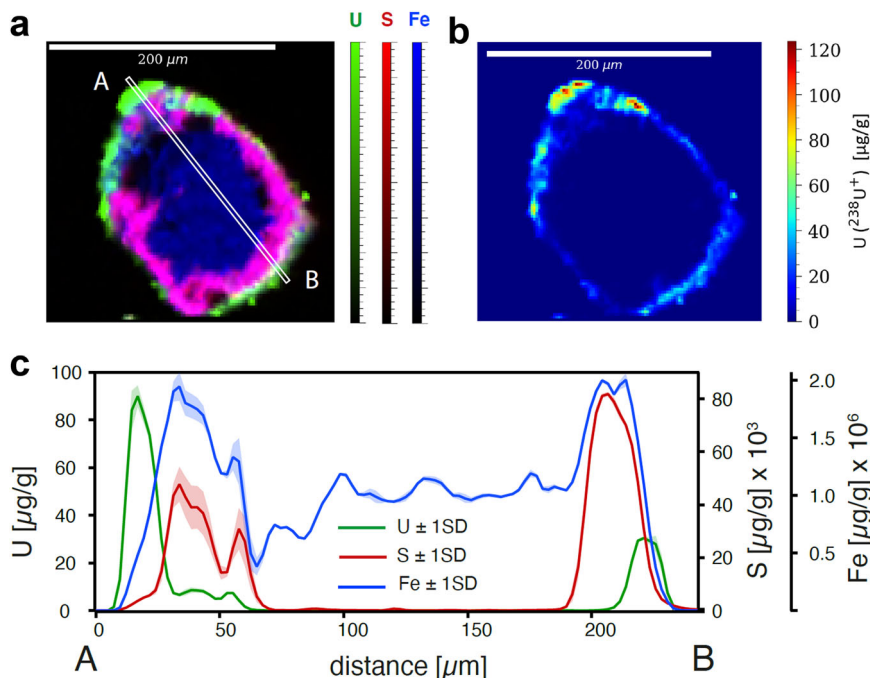
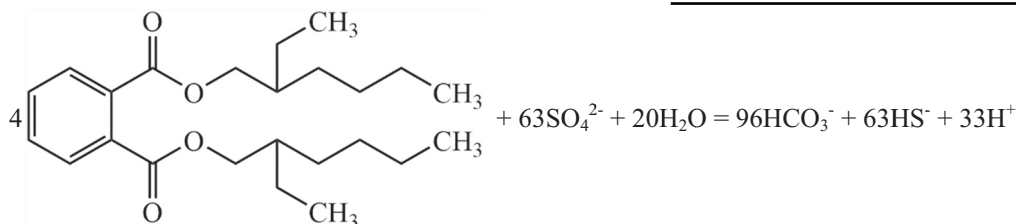


**Fig. 4 Elemental distribution within the mineral grain.** **a** LA-ICP-MS map of U, S, and Fe in sulfidized magnetite (Äspö HRL sample label #22131\_4); **b** U map with several elevated U spots (up to 90 ppm) identified on the grain borders; **c** Transect across grain borders marked as A and B shows the amount of U associated with S and Fe (for details see SI and Supplementary Table 4).

produce carbonate and sulfide while reducing dissolved sulfate in the water, contrary to PVC, which shows meager degradation rates<sup>59</sup>. The stoichiometric reaction shown in Equation 3:



Thus, the degradation of 1 mole of plasticizers results in 24 moles of  $\text{HCO}_3^-$  and nearly 16 moles of  $\text{HS}^-$ , providing the main source of carbonate and sulfides, and promoting precipitation of calcite, amorphous FeS, pyrite, and intermediate species between the latter. Assuming that  $\text{HS}^-_{(\text{aq})}$  occurring at ~0.19 mg/L in the borehole section was constant since the installation of equipment, the total amount of sulfide produced and removed from the borehole section by the flowing groundwater during the last 17 years is 1.13 g (0.034 moles). The amount of tape used in borehole sections provides a sufficient source of DEHP to produce the calculated amount of sulfides. Other mechanisms that can produce sulfide involve the decomposition of dissolved organic carbon (DOC), including low-chain organic compounds present in the fracture water at corresponding depth<sup>60</sup>, such as acetates, and small amounts of ethanol used during drilling campaigns, that are more readily degraded compared to PVC. The degradation of PVC components, in addition to DOC from the incoming groundwater, would be theoretically enough to produce the observed sulfide concentration (0.19 mg/L) in the borehole section (see calculations in SI).

**Isotope fractionation signatures in the groundwater-calcite system.** Removal of U following reduction of U(VI) to U(IV)

species is expected to result in fractionation of primordial  $^{238}\text{U}$  and  $^{235}\text{U}$  isotopes, usually detected both as enrichment of  $^{238}\text{U}$  (positive  $\delta^{238}\text{U}$ ) in the reduced U(IV) phase accumulated on the

surface of redox-active minerals at the rock-groundwater interface, and as depletion of  $^{238}\text{U}$  in the aqueous unreduced residual U fraction as shown for several geological settings<sup>7,8,14</sup>. The U decrease in fracture water versus depth implies that infiltrating U(VI) has undergone reduction, followed by immobilization of U(IV) through multiple removal pathways, as shown above. In the same way, the detected incorporation of U(IV) in the calcite, and the supposed reduction of U(VI) in the borehole water suggests that fractionation between  $^{238}\text{U}$  and  $^{235}\text{U}$  might occur, in agreement with several environmental and laboratory settings<sup>7,8,27,61</sup>. In the Äspö granitoid fracture network, reduction of U(VI) and subsequent precipitation of U(IV) possibly occur along water flow paths, resulting in preferential  $^{238}\text{U}$  removal over  $^{235}\text{U}$  with the lowest measured  $\delta^{238}\text{U} = -2.17\text{‰}$ . The evidence for similar  $\delta^{238}\text{U}$  values measured across roll-front mineral deposits suggests that a similar isotope fractionation pathway might occur in Äspö fracture water<sup>7</sup>. The depleted U that occurs in borehole KA3105A in the form of U(VI)-carbonate complexes is further reduced to U(IV) by  $\text{HS}^-_{(\text{aq})}$  and  $\text{Fe(II)}_{(\text{aq})}$  species results in positive  $\delta^{238}\text{U}$  for longer interaction time<sup>15</sup> and to less extent by  $\text{FeS}_{(\text{nc})}$  (results in depletion of  $^{238}\text{U}$ )<sup>14</sup> formed in situ in borehole sections following calcite precipitation promoted by bacterial activity. The subsequent incorporation of

U(VI) into calcite results in indistinguishable  $^{238}\text{U}$  fractionation between groundwater and calcite with  $\Delta^{238}\text{U}_{\text{calcite-GW}} = (\delta^{238}\text{U}_{\text{calcite}} - \delta^{238}\text{U}_{\text{GW}}) \sim 0\text{‰}$ . The negligible net isotopic fractionation suggests either a kinetically controlled single-step process with no fractionation, or more complex multi-step fractionation routes, including multiple abiotic and microbial redox species, resulting in  $\delta^{238}\text{U}$  varying both in sense and magnitudes, but with a net zero effect. The set of different abiotic ( $\text{HS}^-_{\text{(aq)}}$ ,  $\text{Fe(II)}_{\text{(aq)}}$ , Fe-sulfides) redox species and SRB occurs in the borehole simultaneously and might produce contrasting isotopic signatures that complicate the interpretation of observed U isotope fractionation values<sup>9,15</sup>. Abiotic reduction of U(VI) by  $\text{Fe(II)}_{\text{(aq)}}$  and  $\text{HS}^-_{\text{(aq)}}$  species has been reported to result in positive  $\delta^{238}\text{U}$  (up to 1.7‰), whereas reduction with  $\text{FeS}_{\text{(nc)}}$  results in negligible fractionation<sup>15</sup> to strong  $^{238}\text{U}$  depletion, down to -2.3‰, in the remaining aqueous U(VI) fraction, depending on U speciation<sup>14</sup>. The greatly varying  $\delta^{238}\text{U}$  obtained from the two latter studies for similar systems suggest that there are several key parameters, e.g., U/FeS ratio and U speciation, which depend on Ca content that defines U reduction and removal kinetics, and thus the extent of isotope fractionation.  $\text{Fe(II)}_{\text{(aq)}}$  is a dominant redox species in the stagnant water in section A:3 with ~50% higher concentration (0.29 mg/L) than for  $\text{HS}^-_{\text{(aq)}}$  (0.19 mg/L) along with detected SRB (889–2444 cells/cm<sup>3</sup>) on tape and pipes<sup>47</sup> that might be simultaneously involved into U redox process. The U(VI) redox pathways involving bacterial species may proceed through direct reduction of U(VI) on the surface of bacteria<sup>27,62,63</sup> and indirectly by facilitating the formation of Fe-sulfides capable of substantial U removal<sup>53</sup> that may result in  $\delta^{238}\text{U}$  fractionation of varying sense and magnitude<sup>15</sup>. Due to the relatively low amount of bacteria found on the equipment and in the water<sup>48</sup> at Äspö, a direct association between U and bacteria cannot be unambiguously identified. The FeS removal route supports the previous finding of Fe-sulfides overlying calcite crystals and all parts of the borehole equipment at Äspö HRL<sup>47</sup> with extreme  $^{34}\text{S}/^{32}\text{S}$  fractionation measured in pyrite, thus providing isotopic evidence of SRB activity in the borehole sections<sup>64</sup>. Although the presence of calcite and Ca in groundwater is reported to suppress the removal of U(VI)-carbonates by silicate minerals<sup>65</sup>, Fe-sulfides are expected to hinder U remobilization by fast reduction of U(VI). While  $\text{UO}_2(\text{CO}_3)_3^{4-}_{\text{(aq)}}$  in a Ca-free system can be readily reduced by  $\text{Fe(II)}_{\text{(aq)}}$  species<sup>66</sup> in Ca-rich settings, the dominating  $\text{Ca}_2\text{UO}_2(\text{CO}_3)_3_{\text{(aq)}}$  is a more stable complex that is directly identified in deep aquifer settings even under reducing conditions due to the occurrence of  $\text{Fe(II)}_{\text{(aq)}}$ <sup>67</sup>. A minor effect from U(VI) reduction on FeS might be due to the fact that it is formed later in stagnant water under nearly steady-state conditions<sup>47</sup>. The reduction of U(VI) and subsequent mineralogical removal of U(IV) is not expected to result in notable isotope fractionation due to kinetic effects provided that U(VI) is readily reduced by microbial sulfides in cycles starting with each fracture water inflow event caused by the flushing of the borehole during groundwater sampling. The occurrence of up to 4% of dissolved U(IV) in water may facilitate energetically favorable U incorporation into the calcite structure<sup>11</sup>, with negligible  $\delta^{238}\text{U}$  changes for ambient systems that do not involve U redox processes<sup>3</sup>. Alongside  $\delta^{238}\text{U}$ , the  $^{234}\text{U}/^{238}\text{U}$  (AR) isotopic disequilibrium data can complement the explanation of the observed effects and serve as an isotopic indicator of redox conditions in rock–water systems<sup>14</sup>. The elevated ARs may result from two major mechanisms, involving weathering of the fracture minerals and preferential leaching of alpha-recoiled U fractions<sup>7</sup>. Because significant weathering is not expected in deep anoxic settings where reducing conditions dominate, leaching of recoiled  $^{234}\text{U}$  atoms remains a more preferred pathway creating high AR<sup>68–70</sup>.

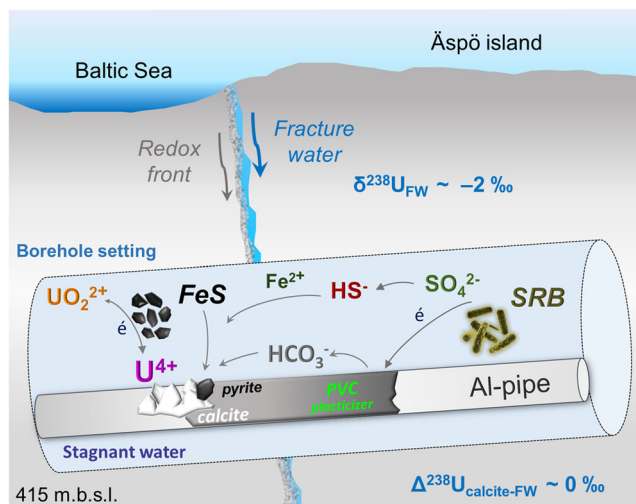


**Fig. 5** A tentative model for U removal and  $\delta^{238}\text{U}$  during U flow in granite fracture network in the Äspö HRL. The degradation of PVC plasticizer is promoted by SRB resulting in the formation of bicarbonate and sulfide. Formation of sulfides in water ( $\text{HS}^-_{\text{(aq)}}$ ) and subsequently as FeS precipitates) is followed by several U removal pathways, including U immobilization on the surface of FeS and pyrite and U(IV) co-precipitation with calcite through structural incorporation.

It is likely that complex mechanisms have affected the observed AR, including multiple U remobilization events.

#### Environmental implications for subsurface anoxic aquifers.

Deep aquifers feature reducing conditions that are largely controlled by organic matter, microorganisms, and abiotic species, such as  $\text{Fe(II)}$ . The latter determines the redox processes involved, and after forming several Fe-oxyhydroxide and/or sulfide phases, alongside calcite<sup>13</sup> it will act as a natural or engineered sink for various trace cations and anions, including natural and artificial radionuclides, e.g., fission products<sup>71</sup> and transuranic elements<sup>25,72</sup>. Based on detailed geochemical and hydrogeological datasets and U isotopic data, we propose a model for U removal and evolution of isotope fractionation as summarized in Fig. 5. Contrary to environments that involve bulk Fe species, e.g., Fe-sulfides and Fe-oxyhydroxides, in low Fe settings the biotic reduction of U(VI) may result in the formation of  $\text{UO}_2$  nanoclusters on mineral or bacterial surfaces<sup>53,63</sup>. More rarely reported is U removal through the formation of U(IV) nanoclusters stabilized in a coffinite-like structure included in Ca carbonate crystals<sup>34</sup>.

Here we report deep aquifer U removal by calcite through structural incorporation of U(IV) and U accumulation on the surface of Fe-sulfides formed on magnetite crystals as a promising process for the sequestration of trace contaminants in the subsurface. In engineered systems, this could be accomplished with low molecular organic matter to produce bicarbonate in addition to conventional biotic remediation strategies for U scavenging, where continuous nutrient injection must be provided to stimulate bacterial activity to maintain U in reduced form. Bacteria promote the degradation of organics that stimulate the formation of calcite and sulfides, followed by reduction of dissolved U(VI) and subsequent immobilization of U(IV).

While calcite is a thermodynamically stable phase under certain environmental settings and oxic conditions, FeS possesses enough sink to scavenge relatively small amounts of oxygen<sup>73</sup> but will oxidize to form elemental sulfur and goethite as ultimate oxidation products during oxygen intrusions<sup>74</sup>. In the case of nuclear waste repositories, particularly those of low-level waste,

cement used for grouting will provide alkaline conditions (pH ~10) that will keep the stability of calcite high, and in addition, in this type of anoxic, circumneutral to slightly alkaline settings, secondary calcite in open water-conducting bedrock fractures have been shown to sustain dissolution for hundreds of millions of years<sup>75–77</sup>. This is much longer than anticipated from laboratory studies and seawater settings<sup>78,79</sup>. Thus, the sequestration of heavy metals in carbonate minerals, such as calcite, mediated by biotic/abiotic redox species, may emerge as an important route to trap toxic wastes, e.g., radioactive species. Specific implications for these U removal processes are obviously deep subsurface repositories for spent nuclear fuel<sup>80</sup>. Although SRB enhances the production of sulfide that can be corrosive to copper canisters encapsulating the spent fuel<sup>81</sup>, we show that SRB can aid in the immobilization of U into secondary mineral sinks that can act in the long-term in subsurface anoxic environments.

## Methods

**Borehole setting and sampling description.** The studied borehole, KA3105A at 415 m depth, was drilled in 1995 into Paleoproterozoic granitoid rock at the Äspö HRL, Sweden, a full-scale test-facility tunnel built and operated by the Swedish Nuclear Fuel and Waste Management Co. (SKB)<sup>82</sup>. The borehole was drilled into the tunnel wall sub-horizontally, with a slight downwards inclination, has a length of 34 m, and was equipped with inflatable pairs of rubber packers, connected by rods of Al running through the whole length of the boreholes. The packer system isolates borehole sections intersected by targeted individuals or clusters of water-conductive fractures from which water can be extracted at the tunnel wall through polyamide tubing for each individual borehole section. A pump is not needed for sampling as groundwater flows spontaneously due to the hydrostatic pressure in the borehole. As a consequence of tunnel excavation, the groundwater in the borehole has a marine signature (as seen in the  $\delta^{18}\text{O}$  and Cl compositions) and is composed of Baltic Seawater mixed with minor proportions of meteoric water and/or older more saline water residing in the bedrock fractures<sup>83</sup>. Calcite and Fe-sulfides crystals observed with no evidence for individual  $\text{UO}_2$  or Fe(III)-oxides on the borehole instrumentation after withdrawal of the packer at the end of a 17-year experiment (1995–2012), were scraped off for laboratory analysis (average thickness of the calcite encrustations 100  $\mu\text{m}$ ) (Supplementary Fig. 1a–d). First, laboratory microscopic analyses showed that calcite, Fe-sulfides, barites, and Al-oxyhydroxides (not analysed by other micro techniques) precipitate together on the borehole equipment. The groundwater in each packed-off section was composed of stagnant water, which was sampled initially when water started to be discharged from the borehole section and may have been affected by the borehole instrumentation, and fracture water collected after discharge of 10 section volumes (59 L in total) and hence represents the pristine groundwater residing in the borehole fractures. Both water types were sampled for chemical analysis by SKB before extraction of the borehole instrumentation in 2012<sup>13,64</sup>. Chemical data for fracture water, collected by SKB from the KA3105A borehole sections, includes four sampling occasions during the 1995–2012 period.

**Microfocus X-ray fluorescence ( $\mu\text{XRF}$ ) and U  $L_{III}$ -edge X-ray absorption near edge structure ( $\mu\text{XANES}$ ).** Selected crystals of calcite were analyzed with  $\mu\text{XRF}$  and U  $L_{III}$ -edge XANES spectroscopy. U  $L_{III}$ -edge  $\mu\text{XANES}$  was recorded at two different microfocus beamlines 4-BM of the National Synchrotron Light Source, NSLS-II, Brookhaven, USA, and microfocus spectroscopy beamline at I18 of the Diamond Light Source, DLS, Harwell, UK<sup>84</sup>. For both beamlines, sample preparation was done in a similar way. Calcite crystals were fixed in between two Kapton tape stripes and positioned at a 45° angle relative to the incident beam. The X-ray beam size at the sample position was focused to 2  $\mu\text{m}$  (vertical)  $\times$  5  $\mu\text{m}$  (horizontal) with Kirkpatrick-Baez mirrors. For  $\mu\text{XRF}$  measurements, an area of  $\sim 150 \mu\text{m} \times 200 \mu\text{m}$  was selected on calcite crystal. Crystal scanning was performed with a step size of 3  $\mu\text{m}$ , 0.2 s integration time, with a total measurement time estimated at 30 min. The energy was calibrated by measuring the peak in first derivatives of K edge XANES spectra of Y foil ( $E_{\text{abs}} = 17.038 \text{ keV}$ ) at I18 (DLS) beamline or Zr foil ( $E_{\text{abs}} = 17.998 \text{ keV}$ ) at 4-BM (NSLS-II) beamline. U  $L_{III}$ -edge  $\mu\text{XANES}$  spectra were collected in a fluorescence mode within the 17,000–17,500 keV range by scanning a Si  $\langle 111 \rangle$  double-crystal monochromator. Several XANES spectra were recorded, 15 min each, until a desired spectral quality of the average of the scans was achieved. To minimize possible beam damage effects, each spectrum was collected at a new position on a U-rich rim area of 30  $\mu\text{m} \times 150 \mu\text{m}$ . Preliminary spectra analysis was done using PyMca software<sup>85</sup>, and normalized with the ATHENA program from DEMETER software package<sup>86</sup>.  $\mu\text{XANES}$  spectra collected at different microfocus beamlines were aligned by comparing the positions of the first inflection points determined for the same calcite material.

U(IV) and U(VI) references. Natural calcite sample reported by Sturchio et al.<sup>11</sup> as used as U(IV) standard for XANES (as U(IV)-calcite). U(VI)-rich calcite material collected from speleothems was used as U(VI) reference

(as U(VI)-calcite)<sup>20</sup> Reference materials were used for U  $L_{III}$ -edge  $\mu\text{XANES}$  spectroscopy according to their availability at 4-BM (NSLS-II, USA) and I18 (DLS, UK) beamlines. The same calcite material was used for both beamlines and spectra were used for the energy correction (Supplementary Fig. 1a, b).

## Extended X-ray absorption fine structure (EXAFS) measurement and data fitting.

U EXAFS measurements were performed at the National Synchrotron Light Source II (NSLS-II), Brookhaven National Laboratory (USA) at beamline 4-BM (XFM). The XFM beamline utilizes an air-bearing fixed-exit Si  $\langle 111 \rangle$  double-crystal monochromator<sup>87</sup>. Calcite crystal was packed into a double layer of 50  $\mu\text{m}$  Kapton tape and mounted on a motorized three-axis sample stage, positioned at 45° to the incident beam. EXAFS spectra were recorded in a fluorescence mode using Canberra SXD-7 SDD coupled to Quantum Detectors Xspress3 DXPs. In total, 122 scans were recorded 20 min per scan in nine discrete spots. Data were extracted, and Fourier transforms were applied over the  $k$ -range 2.5–8.5  $\text{\AA}^{-1}$  using the ATHENA and ARTEMIS programs from the IFFEFIT program package<sup>86</sup>. The fit was performed in  $R$  space for the 1.00–4.10  $\text{\AA}$  range. The scattering paths were generated with the FEFF8.2 code implemented in ARTEMIS using calcite crystal structure (AMCS database no. 0017866). Two short U-O1 and U-O2, one U-C, and long U-O (denoted as U-O3) and one U-Ca single scattering paths (in total, five) were used to fit the EXAFS spectrum. A shell-by-shell modeling approach was followed in the EXAFS analyses. The coordination number of U-C, U-O3, and U-Ca were fixed at 6. The amplitude reduction factor was set to 1. Other parameters were varied.

**Uranium isotope ( $^{238}\text{U}/^{235}\text{U}$ ) measurement.** Samples of calcite were weighed and dissolved in 0.5 M acetic acid and dried down. The samples were then treated with concentrated acetic acid and dried down, before finally bringing them up in 3 M nitric acid. In the case of the groundwater samples, a volume of 100 ml was used for U isotopic analysis. To correct for mass fractionation artefacts due to column chemistry and mass spectrometry, we used a  $^{233}\text{U}$ - $^{236}\text{U}$  mixed-spike, IRMM 3636 (obtained from European Commission Joint Research Inst.) with a  $^{233}\text{U}/^{236}\text{U}$  of 1.01906(16) (2019 ECJRI certificate), to produce a  $^{238}\text{U}/^{236}\text{U}$  ratio of  $\sim 20$ . The  $^{233}\text{U}$ - $^{236}\text{U}$  mixed-spike was added to the aliquots for U isotopic analysis prior to chemical separation, and the mixtures dried down and were taken up in 3 M  $\text{HNO}_3$ , repeating this cycle to insure sample/spike equilibration. Uranium separation from the sample/spike mixtures was conducted using UTEVA resin (Eichrom Technologies) on small Teflon columns following the method described by ref. 88.  $^{238}\text{U}/^{235}\text{U}$  is represented by  $\delta^{238}\text{U}$ , the deviation of the sample  $^{235}\text{U}/^{238}\text{U}$  ratio in parts per thousand from that of the CRM145 U standard. The  $\delta^{235}\text{U}$  values (deviation of the  $^{235}\text{U}/^{238}\text{U}$  from that of CRM145 in parts per thousand) and  $^{234}\text{U}/^{238}\text{U}$  ratios (reported as an activity ratio relative to secular equilibrium, where 1 is secular equilibrium) of the samples were measured using a Neptune (Thermo Fisher), a plasma source multi-collector magnetic sector mass spectrometer housed at Lawrence Berkeley National Lab (Center for Isotope Geochemistry). The estimated external reproducibility ( $2\sigma$ ) of the  $\delta^{238}\text{U}$  measurements is 0.1–0.15‰ based on replicate measurements of CRM112a. Further details of the mass spectrometry method can be found in ref. 14.

## High-resolution laser ablation inductively coupled plasma mass spectrometry (LA-ICP-MS).

LA-ICP-MS mappings were performed at the MAGMA Lab of the TU Berlin using an Agilent 8900 ICP-MS/MS coupled to an Analyte Excite 193 nm excimer laser (Teledyne Photon Machines). Helium is used as a carrier gas with a total flow rate of 0.95 l/min (0.5 l/min cell flow, 0.45 l/min cup flow). After plasma ignition and initialization of Helium flow,  $m/z = 42$  (e.g.,  $^{14}\text{N}^{14}\text{N}^{14}\text{N}^+$ ) and  $m/z = 31$  (e.g.,  $^{15}\text{N}^{16}\text{O}$ ) were recorded to monitor the amount of air entrained in the interface tubing and ablation cell. After counts were stable and below 20000 cps, the Ar nebulizer gas and He carrier gas flows were tuned to achieve  $m/z = 248/232$  ratios of  $< 0.15\%$  (ThO/Th) and  $m/z = 232/238$  ratios of  $100 \pm 1\%$  (Th/U) while ablating NIST 610 in line scan mode. Once stable plasma conditions were reached, an automatic lens tune was performed on NIST 610 to maximize sensitivity in the high mass range. Laser parameters for the tuning were 100 Hz repetition rate, 5  $\mu\text{m}$  square spot size, 50  $\mu\text{m/s}$  scan speed, and 2 J/cm<sup>2</sup> fluence. The resulting gas and plasma parameters are summarized in Supplementary Table 4 and were used for the actual mappings. To reduce sampling time without compromising spatial resolution, the aerosol rapid introduction system ARIS (Teledyne Photon Machines) was used<sup>89</sup>. The single pulse response (SPR), i.e., the combined wash-in and wash-out, was monitored by ablating NIST 612 glass at 1 Hz in line scan mode and recording  $m/z = 238$  (U) with a dwell time of 5 ms. By averaging the peak shape of 300 single pulses, the SPR was determined and was 30 ms (full width at 10% of the maximum intensity). For imaging, the elemental distribution within the target grains, three mass channels  $m/z = 34$  (S),  $m/z = 57$  (Fe), and  $m/z = 238$  (U) were recorded with dwell times of 10 ms each. This resulted in signal-to-noise ratios of  $\sim 200$ ,  $\sim 20,000$ , and  $\sim 2000$ , which were obtained from a single-line scan across one of the target grains. Scan speed and repetition rate were chosen to suppress aliasing artifacts and maximize spatial resolution for the given SPR, dwell times and the spot size of 5  $\mu\text{m}$ . Grains were mapped using a raster of unidirectional scans with no overlap between lines. By applying the above parameters, mapping of a 250  $\times$  250  $\mu\text{m}^2$  area was completed within  $\sim 2$  min. All the raw data processing was performed using the software HDIP (Teledyne Photon machines). The

background was corrected using a cubic spline function. To obtain quantitative mappings, a multi-standard calibration was performed by using multiple line scans on reference materials NIST 612 and BCR-2G recorded before and after the mapping of individual grain. No drift occurred over the short measurement period of <30 min, which was evident from using NIST 612 as a drift monitor.

### Data availability

All relevant data are included in the Supplementary Material of this article and stored publicly available in the archive at Swedish National Data Service ([doris.snd.gu.se](https://doris.snd.gu.se)) and traceable via the article title.

Received: 1 September 2022; Accepted: 20 March 2023;

Published online: 21 April 2023

### References

- Zhang, F. et al. Uranium isotopes in marine carbonates as a global ocean paleoredox proxy: a critical review. *Geochim. Cosmochim. Acta* **287**, 27–49 (2020).
- Bartlett, R. et al. Abrupt global-ocean anoxia during the Late Ordovician–early Silurian detected using uranium isotopes of marine carbonates. *Proc. Natl Acad. Sci. USA* **115**, 5896–5901 (2018).
- Chen, X., Romaniello, S. J., Herrmann, A. D., Samankassou, E. & Anbar, A. D. Biological effects on uranium isotope fractionation ( $^{238}\text{U}/^{235}\text{U}$ ) in primary biogenic carbonates. *Geochim. Cosmochim. Acta* **240**, 1–10 (2018).
- Dahl, T. W. et al. Uranium isotopes distinguish two geochemically distinct stages during the later Cambrian SPICE event. *Earth Planet. Sci. Lett.* **401**, 313–326 (2014).
- Brenneka Gregory, A., Herrmann Achim, D., Algeo Thomas, J. & Anbar Ariel, D. Rapid expansion of oceanic anoxia immediately before the end-Permian mass extinction. *Proc. Natl Acad. Sci. USA* **108**, 17631–17634 (2011).
- Zhang, F. et al. Extensive marine anoxia during the terminal ediacaran period. *Sci. Adv.* **4**, ean8983 (2018).
- Brown, S. T. et al. Isotopic evidence for reductive immobilization of uranium across a roll-front mineral deposit. *Environ. Sci. Technol.* **50**, 6189–6198 (2016).
- Murphy, M. J., Stirling, C. H., Kaltenbach, A., Turner, S. P. & Schaefer, B. F. Fractionation of  $^{238}\text{U}/^{235}\text{U}$  by reduction during low temperature uranium mineralisation processes. *Earth Planet. Sci. Lett.* **388**, 306–317 (2014).
- Bhattacharyya, A. et al. Biogenic non-crystalline U(IV) revealed as major component in uranium ore deposits. *Nat. Commun.* **8**, 15538 (2017).
- Rasbury, E. T. et al. Tools for uranium characterization in carbonate samples: case studies of natural U–Pb geochronology reference materials. *Geochronology* **3**, 103–122 (2021).
- Sturchio, N. C., Antonio, M. R., Soderholm, L., Sutton, S. R. & Brannon, J. C. Tetravalent uranium in calcite. *Science* **281**, 971 (1998).
- Cole, J. M. et al. Petrographic and trace element analysis of uranium-rich tuff calcite, middle Miocene Barstow Formation, California, USA. *Sedimentology* **51**, 433–453 (2004).
- Drake, H. et al. Incorporation of metals into calcite in a deep anoxic granite aquifer. *Environ. Sci. Technol.* **52**, 493–502 (2018).
- Brown, S. T., Basu, A., Ding, X., Christensen, J. N. & DePaolo, D. J. Uranium isotope fractionation by abiotic reductive precipitation. *Proc. Natl Acad. Sci. USA* **115**, 8688 (2018).
- Stylo, M. et al. Uranium isotopes fingerprint biotic reduction. *Proc. Natl. Acad. Sci. USA* **112**, 5619 (2015).
- Magnabosco, C. et al. The biomass and biodiversity of the continental subsurface. *Nat. Geosci.* **11**, 707–717 (2018).
- Drake, H. et al. Biosignatures of ancient microbial life are present across the igneous crust of the Fennoscandian shield. *Commun. Earth Environ.* **2**, 102 (2021).
- Charriau, A. et al. Trace metal behaviour in riverine sediments: Role of organic matter and sulfides. *Appl. Geochem.* **26**, 80–90 (2011).
- Jokinen, S. A., Jilbert, T., Tiihonen-Filppula, R. & Koho, K. Terrestrial organic matter input drives sedimentary trace metal sequestration in a human-impacted boreal estuary. *Sci. Total Environ.* **717**, 137047 (2020).
- Kelly, S. D. et al. Uranyl incorporation in natural calcite. *Environ. Sci. Technol.* **37**, 1284–1287 (2003).
- Kelly, S. D., Rasbury, E. T., Chattopadhyay, S., Kropf, A. J. & Kemner, K. M. Evidence of a stable uranyl site in ancient organic-rich calcite. *Environ. Sci. Technol.* **40**, 2262–2268 (2006).
- Zhang, F. et al. Multiple episodes of extensive marine anoxia linked to global warming and continental weathering following the latest Permian mass extinction. *Sci. Adv.* **4**, e1602921 (2018).
- Livermore, B. D., Dahl, T. W., Bizzarro, M. & Connelly, J. N. Uranium isotope compositions of biogenic carbonates – Implications for U uptake in shells and the application of the paleo-ocean oxygenation proxy. *Geochim. Cosmochim. Acta* **287**, 50–64 (2020).
- Chen, X., Romaniello, S. J., Herrmann, A. D., Wasylenki, L. E. & Anbar, A. D. Uranium isotope fractionation during coprecipitation with aragonite and calcite. *Geochim. Cosmochim. Acta* **188**, 189–207 (2016).
- Heberling, F., Denecke, M. A. & Bosbach, D. Neptunium(V) coprecipitation with calcite. *Environ. Sci. Technol.* **42**, 471–476 (2008).
- Reeder, R. J. et al. Coprecipitation of uranium(VI) with calcite: XAFS, micro-XAS, and luminescence characterization. *Geochim. Cosmochim. Acta* **65**, 3491–3503 (2001).
- Basu, A. et al. Microbial U isotope fractionation depends on the U(VI) reduction rate. *Environ. Sci. Technol.* **54**, 2295–2303 (2020).
- Hudson, E. A., Allen, P. G., Terminello, L. J., Denecke, M. A. & Reich, T. Polarized x-ray-absorption spectroscopy of the uranyl ion: comparison of experiment and theory. *Phys. Rev. B* **54**, 156–165 (1996).
- Burns, P. C., Ewing, R. C. & Hawthorne, F. C. The crystal chemistry of hexavalent uranium; polyhedron geometries, bond-valence parameters, and polymerization of polyhedra. *Canad. Mineral.* **35**, 1551–1570 (1997).
- DePaolo, D. J. Surface kinetic model for isotopic and trace element fractionation during precipitation of calcite from aqueous solutions. *Geochim. Cosmochim. Acta* **75**, 1039–1056 (2011).
- Nielsen, L. C., DePaolo, D. J. & De Yoreo, J. J. Self-consistent ion-by-ion growth model for kinetic isotopic fractionation during calcite precipitation. *Geochim. Cosmochim. Acta* **86**, 166–181 (2012).
- Harfouche, M. et al. EXAFS study of U(VI) uptake by calcium silicate hydrates. *J. Colloid Interface Sci.* **303**, 195–204 (2006).
- Burns, P. C.  $\text{U}^{6+}$  minerals and inorganic compounds: Insights into an expanded structural hierarchy of crystal structures. *Canad. Mineral.* **43**, 1839–1894 (2005).
- Suzuki, Y. et al. Formation and geological sequestration of uranium nanoparticles in deep granitic aquifer. *Sci. Rep.* **6**, 22701 (2016).
- Parkhurst, D. L. & Appelo, C. A. J. Description of input and examples for PHREEQC version 3—A computer program for speciation, batch-reaction, one-dimensional transport, and inverse geochemical calculations. U.S. Geological Survey Techniques and Methods, book 6, ch. A43, 497 p. (2013).
- Neck, V. & Kim, J. I. Solubility and hydrolysis of tetravalent actinides. *Radiochim. Acta* **89**, 1–16 (2001).
- Du, X. et al. Reduction of uranium(VI) by soluble iron(II) conforms with thermodynamic predictions. *Environ. Sci. Technol.* **45**, 4718–4725 (2011).
- WoldeGabriel, G. et al. Characterization of cores from an in-situ recovery mined uranium deposit in Wyoming: implications for post-mining restoration. *Chem. Geol.* **390**, 32–45 (2014).
- Regenspurg, S., Schild, D., Schäfer, T., Huber, F. & Malmström, M. E. Removal of uranium(VI) from the aqueous phase by iron(II) minerals in presence of bicarbonate. *Appl. Geochem.* **24**, 1617–1625 (2009).
- Hua, B., Xu, H., Terry, J. & Deng, B. Kinetics of uranium(VI) reduction by hydrogen sulfide in anoxic aqueous systems. *Environ. Sci. Technol.* **40**, 4666–4671 (2006).
- Jones, B. D. & Ingle, J. D. Evaluation of redox indicators for determining sulfate-reducing and dechlorinating conditions. *Water Res.* **39**, 4343–4354 (2005).
- Zhang, Z. & Furman, A. Soil redox dynamics under dynamic hydrologic regimes - A review. *Sci. Total Environ.* **763**, 143026 (2021).
- Nilsson, A.-C., Gimeno, M. J., Tullborg, E.-L., Mathurin, F. & Smellie, J. Hydrogeochemical data report. Site descriptive modelling Äspö SDM. ISSN 1402-3091, Swedish, Report SKB R-13-26, ID 1396167, Nuclear Fuel and Waste Management Co. (2013).
- Drake, H., Tullborg, E.-L. & MacKenzie, A. B. Detecting the near-surface redox front in crystalline bedrock using fracture mineral distribution, geochemistry and U-series disequilibrium. *Appl. Geochem.* **24**, 1023–1039 (2009).
- Yu, C., Drake, H., Mathurin, F. A. & Åström, M. E. Cerium sequestration and accumulation in fractured crystalline bedrock: the role of Mn-Fe (hydr-)oxides and clay minerals. *Geochim. Cosmochim. Acta* **199**, 370–389 (2017).
- Belli, K. M., DiChristina, T. J., Van Cappellen, P. & Taillefer, M. Effects of aqueous uranyl speciation on the kinetics of microbial uranium reduction. *Geochim. Cosmochim. Acta* **157**, 109–124 (2015).
- Drake, H. et al. Investigation of sulphide production in core-drilled boreholes in Äspö Hard Rock Laboratory. Boreholes KA3110A, KA3385A and KA3105A. ISSN 1404-0344, Report SKB TR-13-12, ID 1403211, Nuclear Fuel and Waste Management Co. (2014).
- Yu, C. et al. Micro-scale isotopic variability of low-temperature pyrite in fractured crystalline bedrock — A large Fe isotope fractionation between  $\text{Fe(II)}_{\text{aq}}$ /pyrite and absence of Fe-S isotope co-variation. *Chem. Geol.* **522**, 192–207 (2019).
- Newsome, L., Morris, K. & Lloyd, J. R. The biogeochemistry and bioremediation of uranium and other priority radionuclides. *Chem. Geol.* **363**, 164–184 (2014).

50. Pan, Z. et al. Nanoscale mechanism of UO<sub>2</sub> formation through uranium reduction by magnetite. *Nat. Commun.* **11**, 4001 (2020).
51. Pidchenko, I. et al. Uranium redox transformations after U(VI) coprecipitation with magnetite nanoparticles. *Environ. Sci. Technol.* **51**, 2217–2225 (2017).
52. Dodge, C. J. et al. Association of uranium with iron oxides typically formed on corroding steel surfaces. *Environ. Sci. Technol.* **36**, 3504–3511 (2002).
53. Gallegos, T. J., Fuller, C. C., Webb, S. M. & Betterton, W. Uranium(VI) interactions with mackinawite in the presence and absence of bicarbonate and oxygen. *Environ. Sci. Technol.* **47**, 7357–7364 (2013).
54. Veeramani, H. et al. Abiotic reductive immobilization of U(VI) by biogenic mackinawite. *Environ. Sci. Technol.* **47**, 2361–2369 (2013).
55. Hyun, S. P., Davis, J. A., Sun, K. & Hayes, K. F. Uranium(VI) reduction by iron(II) monosulfide mackinawite. *Environ. Sci. Technol.* **46**, 3369–3376 (2012).
56. Lee, S. Y. et al. Abiotic reduction of uranium by mackinawite (FeS) biogenerated under sulfate-reducing condition. *J. Radioanal. Nucl. Chem.* **296**, 1311–1319 (2013).
57. Scott, T. B., Riba Tort, O. & Allen, G. C. Aqueous uptake of uranium onto pyrite surfaces; reactivity of fresh versus weathered material. *Geochim. Cosmochim. Acta* **71**, 5044–5053 (2007).
58. Yang, T. et al. Biodegradation of di-(2-ethylhexyl) phthalate by rhodococcus ruber YC-YT1 in contaminated water and soil. *Int. J. Environ. Res. Public Health* **15**, 964 (2018).
59. Quecholac-Piña, X., Hernández-Berriel, M. D., Mañón-Salas, M. D., Espinosa-Valdemar, R. M. & Vázquez-Morillas, A. Degradation of plastics under anaerobic conditions: a short review. *Polymers* **12**, 109 (2020).
60. Osterholz, H. et al. Terrigenous dissolved organic matter persists in the energy-limited deep groundwaters of the Fennoscandian shield. *Nat. Commun.* **13**, 4837 (2022).
61. Stirling, C. H., Andersen, M. B., Warthmann, R. & Halliday, A. N. Isotope fractionation of <sup>238</sup>U and <sup>235</sup>U during biologically-mediated uranium reduction. *Geochim. Cosmochim. Acta* **163**, 200–218 (2015).
62. Abdelouas, A. et al. Biological reduction of uranium in groundwater and subsurface soil. *Sci. Total Environ.* **250**, 21–35 (2000).
63. Suzuki, Y., Kelly, S. D., Kemner, K. M. & Banfield, J. F. Nanometre-size products of uranium bioreduction. *Nature* **419**, 134–134 (2002).
64. Drake, H. et al. Extreme fractionation and micro-scale variation of sulphur isotopes during bacterial sulphate reduction in deep groundwater systems. *Geochim. Cosmochim. Acta* **161**, 1–18 (2015).
65. Dong, W. et al. Influence of calcite and dissolved calcium on uranium(VI) sorption to a Hanford subsurface sediment. *Environ. Sci. Technol.* **39**, 7949–7955 (2005).
66. Dewey, C., Sokaras, D., Kroll, T., Bargar, J. R. & Fendorf, S. Calcium-uranyl-carbonato species kinetically limit U(VI) reduction by Fe(II) and lead to U(V)-bearing ferrihydrite. *Environ. Sci. Technol.* **54**, 6021–6030 (2020).
67. Tullborg, E. L. et al. The occurrences of Ca<sub>2</sub>UO<sub>2</sub>(CO<sub>3</sub>)<sub>3</sub> complex in Fe(II) containing deep groundwater at Forsmark, Eastern Sweden. *Procedia Earth Planet. Sci.* **17**, 440–443 (2017).
68. Ivanovich, M. & Harmon, R. S. *Uranium-series Disequilibrium: Applications to Earth, Marine, and Environmental Sciences* (Clarendon Press, 1992).
69. Tokarev, I. et al. in *Uranium in the Environment: Mining Impact and Consequences* (eds Merkel, B. J. & Hasche-Berger, A.), Origin of high <sup>234</sup>U/<sup>238</sup>U ratio in post-permafrost aquifers (Springer, 2006).
70. Suksi, J. et al. Uranium remobilisation in anoxic deep rock-groundwater system in response to late Quaternary climate changes – Results from Forsmark, Sweden. *Chem. Geol.* **584**, 120551 (2021).
71. Kerisit, S. N. et al. Incorporation modes of iodate in calcite. *Environ. Sci. Technol.* **52**, 5902–5910 (2018).
72. Balboni, E. et al. Plutonium co-precipitation with calcite. *ACS Earth Space Chem.* **5**, 3362–3374 (2021).
73. Bi, Y. & Hayes, K. F. Nano-FeS inhibits UO<sub>2</sub> reoxidation under varied oxic conditions. *Environ. Sci. Technol.* **48**, 632–640 (2014).
74. Chiriță, P., Descostes, M. & Schlegel, M. L. Oxidation of FeS by oxygen-bearing acidic solutions. *J. Colloid Interface Sci.* **321**, 84–95 (2008).
75. Drake, H., Kooijman, E. & Kielman-Schmitt, M. Using <sup>87</sup>Sr/<sup>86</sup>Sr LA-MC-ICP-MS transects within modern and ancient calcite crystals to determine fluid flow events in deep granite fractures. *Geosciences* **10**, 345 (2020).
76. Drake, H. et al. Timing and origin of natural gas accumulation in the Siljan impact structure, Sweden. *Nat. Commun.* **10**, 4736 (2019).
77. Tillberg, M. et al. In situ Rb-Sr dating of slickenfibres in deep crystalline basement faults. *Sci. Rep.* **10**, 562 (2020).
78. Naviaux, J. D. et al. Calcite dissolution rates in seawater: Lab vs. in-situ measurements and inhibition by organic matter. *Marine Chem.* **215**, 103684 (2019).
79. Oelkers, E. H., Golubev, S. V., Pokrovsky, O. S. & Bénézeth, P. Do organic ligands affect calcite dissolution rates? *Geochim. Cosmochim. Acta* **75**, 1799–1813 (2011).
80. Williamson, A. J. et al. Microbial reduction of U(VI) under alkaline conditions: implications for radioactive waste geodisposal. *Environ. Sci. Technol.* **48**, 13549–13556 (2014).
81. Smart, N. et al. Further studies of in situ corrosion testing of miniature copper-cast iron nuclear waste canisters. *Corros. Eng. Sci. Technol.* **46**, 142–147 (2011).
82. Stanfors, R., Rhén, I., Tullborg, E.-L. & Wikberg, P. Overview of geological and hydrogeological conditions of the Äspö hard rock laboratory site. *Appl. Geochem.* **14**, 819–834 (1999).
83. Mathurin, F. A., Åström, M. E., Laaksoharju, M., Kalinowski, B. E. & Tullborg, E.-L. Effect of tunnel excavation on source and mixing of groundwater in a coastal granitoidic fracture network. *Environ. Sci. Technol.* **46**, 12779–12786 (2012).
84. Mosselmans, J. F. W. et al. I18 - the microfocus spectroscopy beamline at the Diamond Light Source. *J. Synchrotron Radiat.* **16**, 818–824 (2009).
85. Solé, V. A., Papillon, E., Cotte, M., Walter, P. & Susini, J. A multiplatform code for the analysis of energy-dispersive X-ray fluorescence spectra. *Spectrochim. Acta B: At. Spectrosc.* **62**, 63–68 (2007).
86. Ravel, B. & Newville, M. ATHENA, ARTEMIS, HEPHAESTUS: data analysis for X-ray absorption spectroscopy using IFEFFIT. *J. Synchrotron Radiat.* **12**, 537–541 (2005).
87. Ding, H. et al. Chemical state mapping of simulant Chernobyl lava-like fuel containing material using micro-focused synchrotron X-ray spectroscopy. *J. Synchrotron Radiat.* **28**, 1672–1683 (2021).
88. Basu, A., Sanford, R. A., Johnson, T. M., Lundstrom, C. C. & Löffler, F. E. Uranium isotopic fractionation factors during U(VI) reduction by bacterial isolates. *Geochim. Cosmochim. Acta* **136**, 100–113 (2014).
89. Van Acker, T. et al. Analytical figures of merit of a low-dispersion aerosol transport system for high-throughput LA-ICP-MS analysis. *J. Anal. At. Spectrom.* **36**, 1201–1209 (2021).
90. Lau, K. V., Romaniello, S. J. & Zhang, F. *The Uranium Isotope Paleo-redox Proxy* (Cambridge Univ. Press, 2019).

## Acknowledgements

I.N.P. is grateful to Horizon2020 Marie Skłodowska-Curie Actions for funding (MITRad project, no. 101024524). K.O.K. acknowledges the support from the European Commission Council under ERC (grant no. 759696). This work was carried out with the support of Diamond Light Source, instrument I18 (proposal SP28254). Portions of this research were also performed at X-ray Fluorescence Microprobe (XFM) and Beamline for Materials Measurement (BMM) beamlines at the National Synchrotron Light Source II, a US Department of Energy (DOE) Office of Science User Facility operated for the DOE Office of Science by Brookhaven National Laboratory under contract no. DE-SC0012704. H.D. acknowledges the following grants, Swedish research council (contracts 2017-05186 and 2021-04365), Formas (contract 2020-01577), and Crafoord foundation (contract 20210524). SKB is thanked for providing access to the Äspö site, to water samples, and hydrochemical data. J.N.C. was supported by the US Department of Energy, Office of Science, Award No. DE-AC02-05CH11231.

## Author contributions

I.N.P. and H.D. designed the study, analysed data, and wrote the manuscript, J.N.C. carried out U and Ca isotope measurements, analysed data and editing, M.K. performed LA-ICP-MS measurements and analysed data, K.I. carried out synchrotron  $\mu$ XRF/ $\mu$ XANES measurements, I.P. performed thermodynamic calculations, E.-L.T., N.M.W.R., and T.S.: conceptualization and editing, E.T.R., P.N., and R.T. provided reference materials, performed  $\mu$ XAS measurements and contributed to discussion, K.O.K. performed HERFD-XANES measurements, Y.S. carried out EMPA measurement and analysed data.

## Funding

Open access funding provided by Linnaeus University.

## Competing interests

The authors declare no competing interests.

## Additional information

**Supplementary information** The online version contains supplementary material available at <https://doi.org/10.1038/s43247-023-00767-9>.

**Correspondence** and requests for materials should be addressed to Ivan N. Pidchenko.

**Peer review information** *Communications Earth & Environment* thanks Benjamin Bostick, Pankaj Pathak and the other, anonymous, reviewer(s) for their contribution to the peer review of this work. Primary Handling Editors: Sadia Ilyas and Joe Aslin.

**Reprints and permission information** is available at <http://www.nature.com/reprints>

**Publisher's note** Springer Nature remains neutral with regard to jurisdictional claims in published maps and institutional affiliations.



**Open Access** This article is licensed under a Creative Commons Attribution 4.0 International License, which permits use, sharing, adaptation, distribution and reproduction in any medium or format, as long as you give appropriate credit to the original author(s) and the source, provide a link to the Creative Commons license, and indicate if changes were made. The images or other third party material in this article are included in the article's Creative Commons license, unless indicated otherwise in a credit line to the material. If material is not included in the article's Creative Commons license and your intended use is not permitted by statutory regulation or exceeds the permitted use, you will need to obtain permission directly from the copyright holder. To view a copy of this license, visit <http://creativecommons.org/licenses/by/4.0/>.

© The Author(s) 2023